PROCEEDINGS A

royalsocietypublishing.org/journal/rspa

Research

Cite this article: Curatolo M, Napoli G, Nardinocchi P, Turzi S. 2021 Dehydration-induced mechanical instabilities in active elastic spherical shells. *Proc. R. Soc. A* **477**: 20210243.
https://doi.org/10.1098/rspa.2021.0243

Received: 15 March 2021
Accepted: 29 September 2021

Subject Areas:
applied mathematics, mathematical physics, materials science

Keywords:
chemo-mechanical instability, bifurcation and buckling, stress-diffusion modelling, soft swelling materials

Author for correspondence:
P. Nardinocchi
e-mail: paola.nardinocchi@uniroma1.it

THE ROYAL SOCIETY
PUBLISHING

Dehydration-induced mechanical instabilities in active elastic spherical shells

M. Curatolo[1], G. Napoli[2], P. Nardinocchi[1] and S. Turzi[3]

[1]Dipartimento di Ingegneria Strutturale e Geotecnica, Sapienza Università di Roma, via Eudossiana, 18, I-00184 Roma, Italy
[2]Dipartimento di Matematica e Fisica 'E. De Giorgi', Università del Salento, Lecce, Italy
[3]Dipartimento di Matematica, Politecnico di Milano, Milano, Italy

MC, 0000-0002-9088-3550; GN, 0000-0002-0539-2686;
PN, 0000-0002-9972-1662; ST, 0000-0003-1245-3800

Active elastic instabilities are common phenomena in the natural world, where they have the character of sudden mechanical morphings. Frequently, the driving force of the instability mechanisms has a chemo-mechanical nature, which makes the instabilities very different from the standard elastic instabilities. In this paper, we describe and study the active elastic instability occurring in a swollen spherical closed shell, confining a water-filled cavity, during a dehydration process. We set up a few numerical experiments based on a stress-diffusion model to give an insight into the phenomenon. Then, we present a study that looks at the chemo-mechanical problem and, through a few simplifying assumptions, allows us to derive a semi-analytical model of the phenomenon. It takes into account both the stress state and the water concentration in the walls of the shell at the onset of the instability. Moreover, it considers the invariance of the cavity volume at the onset of instability, which is due to the impossibility of instantaneously changing the cavity volume filled with water. Eventually, it is shown that the semi-analytic model matches very well the outcomes of the numerical experiments far from the initial regime; the ranges of validity of the approximated analytical model are also discussed.

1. Introduction

Soft capsules confining microscopic cavities are common in Nature. Cavities can be water-filled, as is the case for the fern sporangium [1,2], or not, as is the case for sphagnum moss [3], just to cite a few. In both cases, capsules undergo a dehydration process which determines the conditions for spore dispersion. The working principles of these mechanisms have been classified and studied in terms of the specific functional demands that these mechanisms fulfil [4]. On the contrary, analysing the possibility of reproducing them in soft polymers, which requires accurate modelling and the identification of the determinants of the key mechanism, is still lacking.

Inspired by these observations, we investigate dehydration processes in spherical gel capsules going from a fully wet state with the cavities filled with water towards a dry state when exposed to air. The analysis starts from numerical experiments based on a multi-physics three-dimensional model of stress diffusion [5–9], which shows the onset of mechanical instabilities during the dehydration process. Then, it continues with a study that is set within the chemo-mechanical context and, through a few simplifying assumptions, defines a semi-analytical model which takes into account both the stress state and the water concentration in the walls of the shell at the onset of the instability.

Mechanical instabilities in polymer gels have been extensively studied in recent years with reference to swelling-induced surface instability of confined hydrogel layers on substrates [10–13] and to transient instabilities occurring during swelling processes [6,14–18]. The phenomenon we aim to describe is different and resembles the classical mechanical instabilities of pressurized spherical shells, which have been largely investigated since the 1950s [19–22], and have been recently enjoyed renewed interest [23,24]. However, our problem presents a few aspects that make it distinguishable from the classical ones and motivate our study.

Firstly, in our problem the external pressure, which is the control parameter in the classical stability analyses, is low and insignificant. On the contrary, dehydration processes subject spherical shells to a negative inner pressure, called *suction pressure*, which is an unknown of the stress-diffusion problem, changes in time and can be considered as a live more than a dead load. Hence, load conditions are quite different from those considered in the literature cited above.

Secondly, the driving force of the instability is the drying process, which is controlled by the chemical potential of the environment, that is, the control parameter of the process is not the mechanical pressure. Similar conditions have been studied in [23], where the effects of spontaneous curvature, driven by differential growth, on the instability of spherical shells have been investigated, within the context of the non-Euclidean theory of shells, through a rational approach which allows the spontaneous curvature to be reduced to an effective pressure-like dead load. In [23], it has also been shown as a positive curvature that corresponds to a positive external pressure (or, equivalently, to a negative inner pressure), causing a compression of the shell and possibly also a change in the cavity volume. For dehydrating spherical shells, such as those studied in the present paper, a spontaneous curvature may be identified in terms of the change of dehydration degree across the thickness of the shell. This would result in a positive curvature for the outer layers, which are less hydrated than the inner layers, as the dehydration process starts from the outer layers. However, during the dehydration processes the cavity is filled with liquid, that is, the cavity volume is constrained, and it is expected that the buckling strategy of the shell is affected by the impossibility of changing the cavity volume.

The buckling of elastic spherical shells under osmotic pressure with the osmolyte concentration of the exterior solution as a control parameter has been studied in [25]. Therein, the authors presented a quantitative model that aimed to capture the influence of shell elasticity on the onset of instability. Interestingly, they applied their model under cavity volume control, assuming that the capsule volume can be considered as fixed when it is filled with an incompressible liquid that can leave the cavity on a very slow time scale such as in the drying mechanism. This is the characteristic of our problem, where the instability occurs instantaneously with respect to the times of the diffusion, which can only induce a change in the liquid content of the cavity. However, our model goes beyond this as we present an instability study that is based on the incremental analysis of both the mechanical and chemical equations that govern stress diffusion in polymer gels, and also includes an analysis of the cavity volume constraint.

In particular, after the description of the dehydration process which affects a closed spherical shell in terms of the three-dimensional stress-diffusion model, we evidence and numerically investigate the onset of mechanical instabilities which are driven by the dehydration process. As already discussed, even if instabilities occur when a critical pressure is attained, that pressure is not a control parameter of the instability process, which is driven by the dehydration that is controlled by the chemical potential of the external environment, i.e. the actual control parameter of the dehydration and instability processes. This motivates our choice to analyse the instability problem from a chemo-mechanical perspective through a semi-analytical model, which considers the time evolution of the system state owing to diffusion as a sequence of equilibrium problems; the ranges of validity of the approximation are discussed in appendix A. The stress state and the water concentration in the walls of the shell at the onset of the instability are also demonstrated.

Specifically, our stability analysis is borrowed from the study of elastic thick-walled spherical shells loaded by external pressure presented in [20]. This analysis was also used in a pair of papers in order to characterize growth-induced instabilities in spherical shells [26,27]. However, we extended that analysis to include the effects of water diffusion across the walls of the shell and the invariance of the cavity volume at the onset of instability. We show how the semi-analytic model matches the outcome of the numerical experiments, based on the implementation of the stress-diffusion model, and allows us to have an insight into the mechanical instabilities of the shells numerically investigated and discussed in §3.

2. Chemo-mechanical states of gels

The analysis of dehydration processes starts from swollen gel bodies; however, it is convenient to introduce the dry state $\mathcal{B}_d$ of such bodies, use it as the reference state and describe the chemo-mechanical state of gel bodies by a displacement field $\mathbf{u}_d$ from the dry state and a water concentration c_d per unit dry volume. The displacement $\mathbf{u}_d$ gives the actual position $\mathbf{x} = \mathbf{X}_d + \mathbf{u}_d(X_d, t)$ of a point $\mathbf{X}_d \in \mathcal{B}_d$ at time t, whereas the water concentration c_d gives the moles of water per unit dry volume at $\mathbf{x}$.

We assume that the free energy ψ per unit dry volume depends on the deformation gradient $\mathbf{F}_d = \mathbf{I} + \nabla\mathbf{u}_d$ from $\mathcal{B}_d$ through an elastic component ψ_e, and on the water concentration c_d through a polymer–water mixing energy ψ_m and write $\psi = \psi_e + \psi_m$, as prescribed by the Flory–Rehner thermodynamical model [28,29]. As usual, we assume that any change in volume of the gel is accompanied by an equivalent uptake or release of water content, that is,

$$J_d = \det \mathbf{F}_d = \hat{J}_d(c_d) = 1 + \Omega c_d, \tag{2.1}$$

with Ω (m^3 mol^{-1}) the molar volume of the water. Equation (2.1) introduces a coupling between the state variables of the problem and is usually known as the *volumetric* or *incompressibility* constraint. The volumetric constraint contributes to the definition of a relaxed free energy ψ_r. The latter takes into account the volumetric constraint through the Lagrangian multiplier p and identifies the reaction to the volumetric constraint that maintains the volume change J_d due to the displacement equal to $\hat{J}_d(c_d)$ owing to solvent absorption or release

$$\psi_r(\mathbf{F}_d, c_d, p) = \frac{G_d}{2}(\mathbf{F}_d \cdot \mathbf{F}_d - 3) + \frac{\mathcal{R}T}{\Omega} h(c_d) - p(J_d - \hat{J}_d(c_d)), \tag{2.2}$$

with

$$h(c_d) = \Omega\, c_d \log \frac{\Omega\, c_d}{1 + \Omega\, c_d} + \chi\, \frac{\Omega\, c_d}{1 + \Omega\, c_d}, \tag{2.3}$$

where G_d denotes the shear modulus of the dry polymer and χ the Flory–Rehner parameter whereas $\mathcal{R}$ (J Kmol^{-1}) and T (K) denote the universal gas constant and the ambient temperature, respectively.

Standard thermodynamical processes allow us to derive the constitutive equations for the dry reference stress $\mathbf{S}_d$ (J m^{-3}) (that is, the so-called first Piola–Kirchhoff stress) and for the chemical potential μ (J mol^{-1})

$$\left.\begin{aligned} & \mathbf{S}_d=\hat{\mathbf{S}}_d(\mathbf{F}_d)-p\,\mathbf{F}^{\star}_d = G_d\,\mathbf{F}_d-p\,\mathbf{F}^{\star}_d, \quad \mathbf{F}^{\star}_d=J_d\,\mathbf{F}_d^{-T} \\ \text{and}\qquad & \mu=\hat{\mu}(c_d)+p\,\Omega=\mathcal{R}\,T\left(\log\frac{J_d-1}{J_d}+\frac{1}{J_d}+\frac{\chi}{J_d^2}\right)+p\,\Omega, \end{aligned}\right\} \tag{2.4}$$

where, with a light abuse of notation, we write the relation $\hat{\mu}(c_d)$ for the chemical potential as $\hat{\mu}(J_d)$, by exploiting the volumetric constraint (2.1). Both the stress and chemical potential consist of a constitutively determined component and a reactive component, which couples the two main dynamical subjects of the theory. The components $\hat{\mu}(c_d)$ and $p\,\Omega$ are the mixing and mechanical contribution to the chemical potential.[1]

With these choices, the dissipation principle is reduced to the following inequality:

$$\mathbf{h}_d(\mathbf{F}_d,c_d,p)\cdot\nabla\mu(c_d,p)\le 0, \quad \mu(c_d,p)=\hat{\mu}(c_d)+p\,\Omega, \tag{2.5}$$

where $\mathbf{h}_d$ (mol/(m^2 s)) is the reference solvent flux and is satisfied by assuming that

$$\mathbf{h}_d=\mathbf{h}_d(\mathbf{F}_d,c_d,p)=-\mathbf{M}(\mathbf{F}_d,c_d)\nabla(\hat{\mu}(c_d)+p\,\Omega), \tag{2.6}$$

where the diffusion tensor $\mathbf{M}(\mathbf{F}_d,c_d)$(mol^2/(s m J)) is a symmetric positive-definite strain-dependent tensor. In particular, we also assume that $\mathbf{M}$ is isotropic and linearly dependent on c_d, and diffusion always remains isotropic during any process [5,30–32]. These assumptions determine the representation of the diffusion tensor in terms of the inverse of the Cauchy–Green strain tensor $\mathbf{C}_d=\mathbf{F}_d^T\mathbf{F}_d$,

$$\mathbf{M}(\mathbf{F}_d,c_d)=\frac{D}{\mathcal{R}T}\,c_d\mathbf{C}_d^{-1}, \tag{2.7}$$

where D (m^2 s^{-1}) is the diffusivity. Finally, the balance equations of the model are

$$0=\mathtt{div}\ \mathbf{S}_d \quad\text{and}\quad \dot{c}_d=-\mathtt{div}\ \mathbf{h}_d, \tag{2.8}$$

on $\mathcal{B}_d\times\mathcal{T}$. Therein, a dot denotes the time derivative and `div` the divergence operator. The boundary conditions corresponding to the balance of forces $(2.8)_1$ involve assigned displacements $\bar{\mathbf{u}}$ on $\partial_u\mathcal{B}_d\times\mathcal{T}$ and/or boundary pressure $\bar{p}$ on $\partial_t\mathcal{B}_d\times\mathcal{T}$ and take the form

$$\mathbf{S}_d\,\mathbf{m}=-\bar{p}\mathbf{F}^{\star}_d\mathbf{m} \quad\text{and}\quad \mathbf{u}_d=\bar{\mathbf{u}}, \tag{2.9}$$

respectively, with $\mathbf{m}$ the unit normal to $\partial\mathcal{B}_d$. On the other hand, the boundary conditions corresponding to the balance of liquid mass $(2.8)_2$ involve the boundary flux q_s on $\partial_q\mathcal{B}_d\times\mathcal{T}$ and/or the concentration field c_s on $\partial_c\mathcal{B}_d\times\mathcal{T}$, which are implicitly assigned by controlling the external chemical potential μ_e on $\partial_c\mathcal{B}_d\times\mathcal{T}$; they take the form

$$-\,\mathbf{h}_d\cdot\mathbf{m}=q_s \quad\text{and}\quad \hat{\mu}(c_s)+p\,\Omega=\mu_e. \tag{2.10}$$

The initial conditions

$$\mathbf{u}_d=\mathbf{u}_{do} \quad\text{and}\quad c_d=c_{do} \tag{2.11}$$

on $\mathcal{B}_d\times\{0\}$ make the problem solvable: $\mathbf{u}_{do}$ and c_{do} are the initial values of the fields $\mathbf{u}_d$ and c_d, respectively.

(a) Dehydration of gel capsules

We discuss dehydration of spherical shells confining spherical cavities. The dry system $\mathcal{B}_d$ is a spherical shell of external radius R_d and thickness $H_d=R_d-R_c$, with R_c the radius of the cavity

---

[1] The term $\hat{\mu}(c_d)/\Omega$ (J m^{-3}) is a pressure that is usually called the *osmotic pressure* in contrast with the p term, which is called the *mechanical contribution to the chemical potential* as evidenced by rewriting equation $(2.4)_2$ in the form

$$\frac{\mu}{\Omega}=\frac{\mathcal{R}T}{\Omega}\left(\log\frac{J_d-1}{J_d}+\frac{1}{J_d}+\frac{\chi}{J_d^2}\right)+p.$$

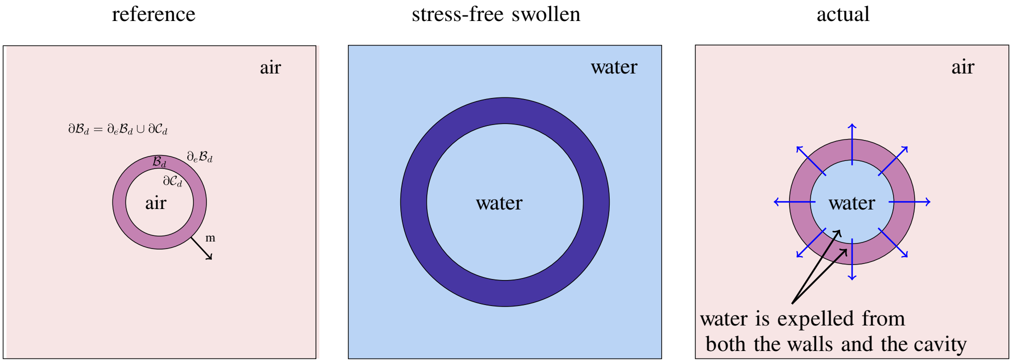

Figure 1. A sketch of the dehydration process. Dry state of the spherical capsule (*a*). Initial steady stress-free swollen state of the spherical capsule: water fills the cavity and the external environment (*b*). After exposure to air, the dehydration process starts and water is expelled from both the walls and the cavity (*c*). (Online version in colour.)

$\mathcal{C}_d$; the ratio H_d/R_c is a measure of the thinness of the shell. When the capsule is immersed in water, the shell size increases to accomodate an amount of water which is determined by the ratio m between the shear modulus G_d and the chemical energy density per unit volume $\mathcal{R}T/\Omega$, if the Flory parameter χ has been fixed, through the equation

$$\log\frac{\lambda_o^3-1}{\lambda_o^3}+\frac{1}{\lambda_o^3}+\frac{\chi}{\lambda_o^6}+\frac{m}{\lambda_o}=\bar{\mu}_o,\quad \text{with}\quad m=\frac{G_d\Omega}{\mathcal{R}T}\quad\text{and}\quad \bar{\mu}_o=\frac{\mu_o}{\mathcal{R}T}. \tag{2.12}$$

Equation (2.12) corresponds to the equilibrium conditions $\mathbf{S}_d=\mathbf{0}$ and $\mu=\mu_e$ with μ_e equal to an initial value μ_o. With this, the balance equations (2.8) are trivially satisfied and we denote this steady and stress-free swollen state as $\mathcal{B}_o$. At $\mathcal{B}_o$, the shell has radius $\lambda_o R_d$ whereas the cavity $\mathcal{C}_o$, assumed to be completely filled with water, has radius $\lambda_o R_c$ and the shell has thickness $H_o=\lambda_o(R_d-R_c)$.

We assume that this state represents the initial state of the system under a dehydration process which starts from the fully swollen state $\mathcal{B}_o$ and proceeds by dehydrating the body from the outside. This corresponds to pulling out the swollen spherical shells, with their cavities filled with water, from the bath and exposing them to air (figure 1). Diffusion starts and water is expelled from both the gel and the cavity. As water is incompressible, the cavity volume must always be equal to the volume of the water it contains; thus, when water is pumped out of the cavity, the cavity volume reduces and the cavity wall $\partial_i\mathcal{B}_d=\partial\mathcal{C}_d$ may be pulled by an increasing negative pressure.

From the modelling point of view, exposing the capsule to air means changing the chemical potential at the external boundary $\partial_e\mathcal{B}_d$ from μ_o to $\mu_e<\mu_o$. If this is the case, equations (2.8)–(2.11) allow the dynamics of the process to be followed. We assume that throughout the process the cavity is always filled with solvent[2] and the chemical potential on $\partial_i\mathcal{B}_d$ is determined by the value it has in pure water, that is, $\mu_i=\mu_o+\Omega\, p_i(t)$ with the pressure term p_i representing the suction pressure. In contrast, we assume that the outer environment is filled with air, that is, an ideal gas whose content in water determines the value of the chemical potential, which can be related to the relative humidity of the air, and set $\mu_e=\hat{\mu}_e(t)+p_e$ with $\hat{\mu}_e(t)$ the control law of the problem and the base atmospheric pressure $p_e=0$. Figure 2*c* shows the control law $\hat{\mu}_e(t)$, which starts from an initial value $\mu_o=0$ and takes a final value μ_f in a prescribed time. So, in the end, we write

$$\mu_e=\hat{\mu}_e(t)\quad\text{on } \partial_e\mathcal{B}_d\quad\text{and}\quad \mu_i=\Omega\, p_i(t)\quad\text{on}\quad \partial\mathcal{C}_d \tag{2.13}$$

---

[2] This corresponds to assuming that no delamination of liquid from the cavity walls can occur, or, equivalently, that the surface energy per unit area of the cavity is much higher than the stretching modulus $G\lambda_o(R_d-R_c)$.

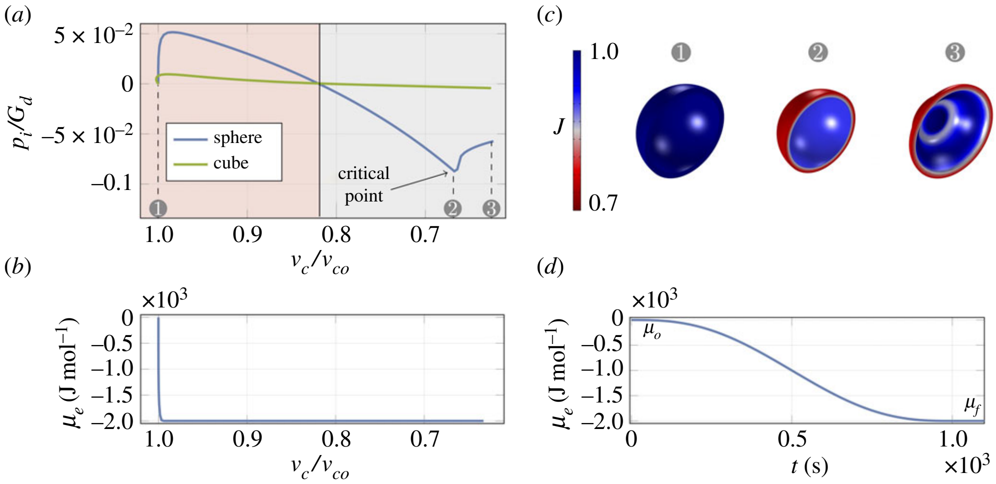

Figure 2. Pressure–volume curves for spherical (blue) and cubic (green) gel capsules: pink (grey) background identifies the phase of the process when the inner pressure takes positive (negative) values (*a*). Pattern of the external chemical potential μ_e versus v_c/v_{co} (*b*). Shapes of the spherical capsules at different values of $v_c/v_{co} = 1, 0.68, 0.65$ (*c*). Pattern of the external chemical potential μ_e versus time: this decreases from the initial value $\mu_o = 0\ \mathrm{J\ mol^{-1}}$ to the final value $\mu_f = -2 \times 10^3$, which is attained in about 10^3 s (*d*). (Online version in colour.)

and

$$\mathbf{S}_d\,\mathbf{m} = -p_e\,\mathbf{F}_d^\star\,\mathbf{m} = \mathbf{0} \quad \text{on } \partial_e\mathcal{B}_d \times \mathcal{T} \quad \text{and} \quad \mathbf{S}_d\,\mathbf{m} = -p_i\,\mathbf{F}_d^\star\,\mathbf{m} \quad \text{on } \partial\mathcal{C}_d \times \mathcal{T}, \tag{2.14}$$

where $\mathbf{F}_d^\star = J_d\mathbf{F}_d^{-T}$ denotes the adjugate of the deformation gradient. A new equilibrium state is attained when $\mu = \mu_e = \mu_i$ across the thickness of the shell and the field $\mathbf{h}_d = \mathbf{0}$. The time τ_e required to achieve the new steady state depends on the diffusivity constant D of the system or, equivalently, on the characteristic diffusion time $\tau_d = H_o^2/D$: higher is D, smaller is τ_e.

The suction pressure $p_i = p_i(t)$, a key ingredient in the onset of instabilities, is modelled as the reaction to the volumetric coupling relating the volume $v_s^c = v_s^c(t)$ of the solvent in the cavity to the volume of the cavity $v_c = v_c(t)$: at each instant $t \in \mathcal{T}$ as solvent flows out of the cavity; it, therefore, holds that

$$v_c(t) = v_s^c(t). \tag{2.15}$$

It is worth noting that the global constraint (2.15) adds a further coupling between the state variables of the multiphysics problem other than the common local volumetric constraint (2.1). Constraint (2.15) can be enforced by considering the augmented total free energy, defined by

$$\int_{\mathcal{B}_d} \psi_r\, dV_d - p_i\,(v_c - v_s^c), \tag{2.16}$$

so that the cavity pressure p_i can be viewed as the Lagrange multiplier enforcing the constraint. The cavity volume v_c depends on the actual configuration $\mathcal{C}_t$ of the cavity at time t, and can be computed via Nanson's formula by evaluating the following integral:

$$v_c(t) = \int_{\mathcal{C}_t} dv = -\frac{1}{3}\int_{\partial_i\mathcal{B}(t)} \mathbf{x}\cdot\mathbf{n}\,\mathrm{d}a = -\frac{1}{3}\int_{\partial_i\mathcal{B}_d} (\mathbf{X}_d + \mathbf{u}_d)\cdot\mathbf{F}_d^\star\,\mathbf{m}\,\mathrm{d}A_d, \tag{2.17}$$

with $\mathbf{n}$ the normal to the actual boundary $\partial_i\mathcal{B}(t) = f(\partial\mathcal{C}_d)$.[3] The water volume at time t is the sum of the initial water content $v_s^c(0)$ of the cavity, plus the water volume $Q_i(t)$ that crosses the cavity

---

[3] We note that the internal boundary of the gel $\partial_i\mathcal{B}_d$ coincides with the boundary of the cavity $\partial\mathcal{C}_d$, with the proviso that the unit normal has an opposite orientation.

boundary during the time interval $(0, t)$, that is, $v_s^c(t) = v_s^c(0) + Q_i(t)$. The initial water content equals the initial cavity volume $v_{co} = v_c(0)$, that is, from (2.17), it holds that

$$v_s^c(0) = v_c(0) = -\frac{1}{3}\int_{\partial_i \mathcal{B}_d} (\mathbf{X}_d + \mathbf{u}_o) \cdot \mathbf{F}_o^\star \, \mathbf{m} \, \mathrm{d}A_d, \tag{2.18}$$

with $\mathbf{F}_o^\star = J_o \, \mathbf{F}_o^{-T}$ and J_o the adjugate and the Jacobian determinant of the initial swollen deformation gradient $\mathbf{F}_o = \lambda_o \mathbf{I}$. The water volume $Q_i(t)$ that crosses the cavity boundary and is absorbed by the gel can be evaluated by

$$Q_i(t) = \int_0^t \dot{Q}_i(\tau) \, \mathrm{d}\tau = \Omega \int_0^t \left(\int_{\partial_i \mathcal{B}_d} q \, \mathrm{d}A_d \right) \mathrm{d}\tau = -\Omega \int_0^t \left(\int_{\partial_i \mathcal{B}_d} \mathbf{h}_d \cdot \mathbf{m} \, \mathrm{d}A_d \right) \mathrm{d}\tau. \tag{2.19}$$

Equations (2.17)–(2.19) allow us to follow the dehydration process of the spherical capsule. It is worth noting that the effects of the process on the mechanics of the shell are very different depending on the shear modulus of the polymer. High- or low-shear moduli G_d identify the initial state $\mathcal{B}_o$ as a poorly or highly swollen state and, with fixed D, can determine a very different dynamics [8,33]. For highly swollen gels, owing to the large amount of liquid inside shell walls, the dehydration process starts with the liquid first released from the shell rather than from the cavity. As a consequence, the suction effect does not become immediately apparent and the inner pressure p_i takes non-negative values. By contrast, for poorly swollen gels, liquid is mainly released from the cavity and the inner pressure quickly attains negative values [33], a condition which is the determinant for the onset of mechanical instabilities, as we will discuss in the rest of the paper.

3. A glance at active elastic instabilities

The effects of the dehydration process on shell shape are numerically studied and the onset of the so-called *active elastic* instabilities is investigated.

We set up a series of numerical experiments based on a finite-element model successfully tested in different situations [5–9]. Our finite-element model solves the balance equations in integral form (weak form) together with the volumetric constraints and boundary conditions. Then, the full problem can be reformulated as follows: find $\mathbf{u}_d$, c_d, p, p_i and c_s (an auxiliary concentration variable used in the chemical boundary conditions) such that, for any test functions $\tilde{\mathbf{u}}_d, \tilde{c}_d, \tilde{p}, \tilde{p}_i$ and $\tilde{c}_s$, balance equations (2.8), volumetric constraints (2.1), (2.15), boundary conditions (2.13), (2.14) and initial conditions (2.11) in weak formulation hold. We used tetrahedral elements to discretize the three-dimensional body and more specifically approximately 500 domain elements are used with 20 000 degrees of freedom. The convergence of the model is obtained with cubic-order Lagrange shape functions for the balance of forces, a quartic-order Lagrange shape function for the balance of the solvent mass and a quadratic nodal serendipity shape function for the Lagrangian multiplier of the volumetric constraint equation. It is worth noting that high orders of shape functions are also mandatory to obtain good accuracy as both the dependent variables $\mathbf{u}_d$ and c_d in the balance laws have second spatial derivatives.

We fixed the set of material parameters listed in table 1. With these choices, the dimensionless parameter $m = G_d \Omega / RT$ is around 0.37. The value of $m \gtrsim 10^{-1}$ and of the affinity parameter $\chi \lesssim 0.8$ allows us to infer that the gel is poorly swollen.

Indeed, with fixed $\mu_o = 0\,\mathrm{J\ mol^{-1}}$, equation (2.12) yields the value $\lambda_o = 1.152$ for the swelling ratio. This corresponds to a 15% increase in the capsule thickness and radius, which change from the dry values $H_d = 1.25 \times 10^{-3}$ m and $R_d = 1 \times 10^{-2}$ m to the swollen values $H_o = 1.44 \times 10^{-3}$ m and $R_o = 1.152 \times 10^{-2}$ m. The corresponding initial values for the displacement and pressure field are $\mathbf{u}_o = (\lambda_o - 1)\mathbf{X}_d$ and $p_o = 4.338 \times 10^7$ Pa. From the value μ_o, the chemical potential is made to change following a time law $\hat{\mu}_e(t)$, which brings the value of the external chemical potential from the initial value μ_0 to the final value $\mu_f = -2 \times 10^3$ J/mol in a time $\tau_\mu = 1000$ s through a smoothed step function; then, the final value μ_f is kept fixed (figure 2*d*).

Table 1. Values of parameters used in numerical experiments; the particular values for χ and G_d assume a good affinity between the polymer and solvent, which is standard for gels and water, and a quite stiff gel [34].

shear modulus	$G_d = 5 \times 10^7$ Pa
Flory parameter	$\chi = 0.2$
water molar volume	$\Omega = 1.8 \times 10^{-5}$ m^3 mol^{-1}
water diffusivity	$D = 10^{-9}$ m^2 s^{-1}
temperature	$T = 293$ K

The dimensionless pressure–volume p_i/G_d versus v_c/v_{co} curves shown in figure 2*a* allow us to highlight the observed dynamics in spherical capsules (blue line) and to evidence the onset of a mechanical instability that is, on the contrary, not observed in cubic capsules of similar size (green line). At the beginning of the dehydration process from the swollen shell, liquid is mainly expelled from the cavity walls and pressure changes at almost unchanged cavity volume, as the initial deep slope of the blue line shows. As diffusion continues, water is released from both the shells and the cavity and the cavity volume reduces; we follow this until a decrease of about 30% is attained, corresponding to $v_c/v_{co} \simeq 0.7$. In the first phase (pink background), the inner pressure takes positive values, which, at the same v_c/v_{co}, are higher for spherical than for cubic capsules, and breathing modes can be observed in both the situations [8]. In the second phase (grey background), the inner pressure takes negative values, so realizing the so-called suction effect on the walls of the capsules. Whereas the walls of the cubic capsules bend under negative pressure, spherical capsules, made stiffer by the geometrical symmetry, do not bend, as is shown in figure 2*b* by the number 2. Moreover, as it is energetically very expensive to reduce cavity volume in spherical capsules, we also observe higher values of the negative pressure at the same value of the ratio v_c/v_{co} in spherical than in cubic capsules.

The numerical analysis identifies the critical value of the inner pressure at which the mechanical instability, which allows the shell to release the elastic energy stored during the process, is observed. The onset of the mechanical instability changes the shape of the sphere very sharply and the pressure–volume curve shows an almost vertical slope at the critical point, as is evidenced in figure 2*a*, corresponding to the ramp of the external chemical potential shown in figure 2*b*. Indeed, as the cavity is still filled with water, and diffusion is slow (here, the characteristic diffusion time $\tau_d = H_o^2/D \simeq 2 \times 10^3$ s), instability occurs at almost constant volume. Figure 2*b* also shows the spherical capsule at different values of $v_c/v_{co} = 1, 0.68, 0.65$, corresponding to the points $1, 2, 3$ shown in the pressure–volume diagram. At the value $v_c/v_{co} = 0.65$ (point 3), the spherical capsule has attained a *sombrero* shape. Key determinants of the mechanical instability are the cavity volume ratio v_c/v_{co} and the inner pressure p_i. In particular, we observe that the onset of instability corresponds to a pair $v_c/v_{co} = 0.68$ and $p_i = -4.2 \times 10^6$ Pa. These values will be used as benchmark values in the following section, where a semi-analytical study of the instability is presented.

4. Study of the chemo-mechanical instability

The key aspects of the instability problem, which affect spherical shells during dehydration processes, can be described from a mechanics perspective through a few simplifying assumptions which allow us to derive a semi-analytical model. The proposed stability analysis is borrowed from the study of elastic thick-walled spherical shells loaded by external pressure presented in [20], and is extended to consider the diffusion equation $(2.8)_2$ and the global constraint equation (2.15).

As diffusivity is small and we look at the solution for $t \ll \tau_e$ and $t > \tau_\mu$, we approximate the dynamical process as a sequence of equilibrium states over sufficiently small time intervals $\Delta t \ll \tau_d$. Over each interval, the volume cavity and the flux do not change with time and this allows us to solve the problem as a quasi-static problem where the cavity volume is prescribed. In other words, as the cavity is still filled with water and diffusion is typically a slow process, instability occurs at almost constant volume, that is, as if diffusion was *frozen*. More details of this approximation are discussed in appendix A.

(a) Spherical solution

Before instability occurs, the shell is spherical and the chemo-mechanical state variables are determined as solutions of equations (2.8) within the quasi-static approximation. Assuming the dry configuration as the reference configuration, we consider purely radial deformations of the thick shell and represent them as

$$r = r(R), \quad \theta = \Theta, \quad \phi = \Phi, \tag{4.1}$$

where (R, Θ, Φ) and (r, θ, ϕ) are the spherical coordinates of a point in the reference and current configuration, respectively. We denote all the chemo-mechanical variables corresponding to the spherical solution with the subscript '0'; so $\mathbf{F}_0 = \mathrm{diag}(r', r/R, r/R)$ is the deformation gradient corresponding to the deformation (4.1), with a prime denoting differentiation with respect to the radial coordinate R. The equilibrium configurations have to satisfy the volumetric constraint (2.1): $\det \mathbf{F}_0 = J_0(R)$, with $J_0(R) = 1 + \Omega c_0(R)$, where c_0 denotes the solvent concentration in the spherical solution. When we substitute (4.1) into the constraint, we get

$$r^2 r' = R^2 J_0. \tag{4.2}$$

Note that unlike the classical analysis [20,35], where $J_0 = 1$, here J_0 is an unknown function of the radial coordinate. When $J_0 = 1$, equation (4.2) can be easily solved and yields the classical result $r(R) = (a_0 + R^3)^{1/3}$, where a_0 is an integration constant. By contrast, in our case, equation (4.2) has to be solved together with the chemo-mechanical balance equations.

Let us introduce $Q_0(R) := R/r(R)$ so that the deformation gradient of the spherical solution can be cast in the form

$$\mathbf{F}_0 = \mathrm{diag}(Q_0^2 J_0, Q_0^{-1}, Q_0^{-1}). \tag{4.3}$$

Then, according to the neo-Hookean hyperelastic model, the Piola–Kirchhoff stress tensor can be written as

$$\mathbf{S}_0 = \mathrm{diag}(-p_0 Q_0^{-2} + G_d J_0 Q_0^2, -p_0 J_0 Q_0 + G_d Q_0^{-1}, -p_0 J_0 Q_0 + G_d Q_0^{-1}), \tag{4.4}$$

where $p_0(R)$ is the Lagrangian multiplier related to the constraint $J_0 = 1 + \Omega c_0$. On the other hand, the representation formula of the chemical potential is unchanged by the spherical symmetry and it holds that

$$\mu_0 = \mathcal{R}\,T\left(\log\frac{J_0 - 1}{J_0} + \frac{1}{J_0} + \frac{\chi}{J_0^2}\right) + p_0\,\Omega. \tag{4.5}$$

Observing that $Q_0' = Q_0(1 - J_0 Q_0^3)R^{-1}$, the balance of forces $\texttt{div}\,\mathbf{S}_0 = \mathbf{0}$ (in spherical coordinates, $R\partial_R S_{0_{RR}} + 2S_{0_{RR}} - S_{0_{\Theta\Theta}} - S_{0_{\phi\phi}} = 0$) reduces to

$$p_0' R + 2G_d Q_0(-1 + J_0 Q_0^3)^2 - G_d Q_0^4 J_0' R = 0. \tag{4.6}$$

As far as the diffusion problem is concerned, we assume that the quasi-static version of $(2.8)_2$ holds, that is, $\texttt{div}\,\mathbf{h}_0 = 0$.

Owing to the spherical symmetry, the solvent flux $\mathbf{h}_0$ is purely radial, that is, $\mathbf{h}_0(R) = (h_{0_R}(R), 0, 0)$, and the balance equation, after a first integration, reduces to

$$R^2 h_{0_R} = C_0, \tag{4.7}$$

where C_0 is an integration constant, while the constitutive equations (2.6) and (2.7), reduced by the spherical symmetry, give

$$h_{0_R} = -\frac{D}{Q_0^4 J_0^2}\left[\frac{-2\chi(J_0 - 1) + J_0}{\Omega J_0^3} J_0' + \frac{(J_0 - 1)}{\mathcal{R}T} p_0'\right]. \tag{4.8}$$

Finally, by using the boundary conditions (2.13) and (2.14), we obtain the boundary conditions for the spherical problem

$$S_{0_{RR}}(R_d) = 0, \quad \mu(R_d) = \mu_f \tag{4.9a}$$

and

$$\mu(R_c) + \Omega Q_0^2(R_c) S_{0_{RR}}(R_c) = 0\,. \tag{4.9b}$$

Equation (4.9*a*) expresses the conditions of vanishing pressure and assigned chemical potential at the external boundary equal to the final value μ_f attained by μ_e. Equation (4.9*b*) is derived from $(2.13)_2$, which relates the chemical potential $\mu(R_c)$ and the pressure p_i on the inner boundary, where the boundary condition $(2.14)_2$ has been used to express p_i in terms of the radial stress component as $p_i = -Q_0^2(R_c) S_{0_{RR}}(R_c)$.

Finally, it is worth noting that, at any time before instability occurs, the enclosed volume v_c is determined by the liquid filling the cavity and the relationship between the radius r_c of the cavity and the volume v_c is

$$r_c = \left(\frac{3v_c}{4\pi}\right)^{1/3}. \tag{4.10}$$

Hence, as the cavity volume is assigned, equation (4.10) delivers the fourth boundary condition

$$r(R_c) = r_c. \tag{4.11}$$

If $\mu_e = 0$ J/mol and the cavity volume is not constrained, this spherical problem admits the stress-free *swollen solution* discussed in §2, which leads to the uniform deformation $\lambda_o = Q_0^{-1} = J_0^{1/3}$, where λ_o satisfies equation (2.12). The corresponding enclosed volume is then $v_{co} = \frac{4}{3}\pi R_c^3 J_0$.

For any cavity volume v_c different from the initial value v_{co}, the solution $(p_0(R), J_0(R), r(R))$ of the spherical problem and the integration constant C_0 are determined by equations (4.2), (4.6), (4.7) and (4.8), with the boundary conditions (4.9) and (4.11).

Let us introduce the symbol

$$\beta := \frac{v_c}{v_{co}}, \tag{4.12}$$

that is, the ratio between the current and the initial volume of the cavity, which is a key parameter of the successive stability analysis. The solution above allows us to draw the relationship between the inner pressure p_i and β and to evaluate the concentration and the chemical potential fields across the shell thickness.

Figure 3*a* shows the dimensionless inner pressure p_i/G_d versus β lines from analytics (black) and from numerics (blue) for $\tau_d = 2 \times 10^3$ s. It is worth noting that the black line matches very well the numerical line apart from the initial transient when the pressure–β slope is high and $\beta \simeq 1$, corresponding to water released from the external walls. During that transient the external chemical potential takes values between μ_o and μ_f (figure 2*a*,*b*) and the analytical model cannot reproduce that transient, as it solves the problem under the boundary condition $(4.9a)_2$. Figure 3*b* and figure 3*c* compare the pattern of c_d and μ at $\beta = 0.68$ and show that the quasi-static solution satisfactorily matches the numerical solution arising from the dynamical analysis even if we are far from the thermodynamical equilibrium state, as the chemical potential is not uniform across the shell thickness. Finally, figure 3*d* shows local volume changes across the shell thickness, as obtained from analytics for different values of the parameter m. We observe that, as m increases, the change in volume, and hence the absorption capacity of the shell, decreases. The purely elastic limit can be obtained for larger and larger values of m.

(b) The linearized problem

In order to find the critical values of β at which the instability occurs, we consider the incremental fields u, v, p_1, J_1 and write

$$\mathbf{x}(R,\Theta) = r(R)\mathbf{e}_R + \epsilon(u(R,\Theta)\mathbf{e}_R + v(R,\Theta)\mathbf{e}_\Theta), \tag{4.13a}$$

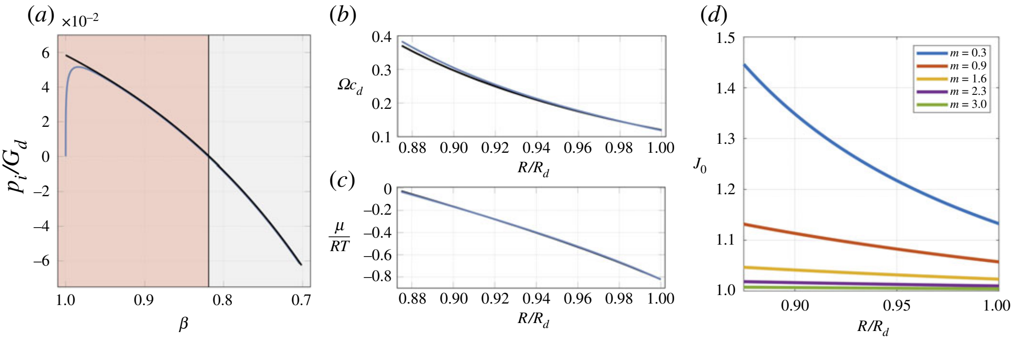

Figure 3. Dimensionless inner pressure p_i/G_d versus β lines from analytics (black) and numerics (blue) for $\tau_d = 2 \times 10^3$ s and $R_c/R_d = 0.87$ (*a*). Water concentration and dimensionless chemical potential across the shell thickness from analytics and from numerics at $\beta = 0.68$ (*b*,*c*). Local volume change J_0 across the shell thickness for several values of $m = G_d\Omega/\mathcal{R}\,T$ (*d*). (Online version in colour.)

$$p(R,\Theta) = p_0(R) + \epsilon p_1(R,\Theta) \tag{4.13b}$$

and

$$J_d(R,\Theta) = J_0(R) + \epsilon J_1(R,\Theta). \tag{4.13c}$$

This ansatz takes into account axisymmetric perturbations and neglects possible displacements in the azimuthal direction. However, as shown in [20,27], this is not restrictive since the incremental equations are independent of the azimuthal wavenumber.

Therefore, the incremental deformation gradient is

$$\mathbf{F}_1 = \begin{pmatrix} \partial_R u & R^{-1}(\partial_R u - v) & 0 \\ \partial_R v & R^{-1}(u + \partial_\Theta v) & 0 \\ 0 & 0 & R^{-1}(u + v\cot\Theta) \end{pmatrix}, \tag{4.14}$$

and the unknown fields u and v have to satisfy the volumetric constraint, which at first order is $J_0\,\mathrm{tr}(\mathbf{F}_0^{-1}\mathbf{F}_1) = J_1$ and can be written as

$$Q_0^{-2}\,\partial_R u + J_0 Q_0 R^{-1}(2u + \partial_\Theta v + v\cot\Theta) - J_1 = 0. \tag{4.15}$$

This equation has to be coupled with the incremental equilibrium equations

$$\mathtt{div}\ \mathbf{S}_1 = 0 \quad \text{and } \mathtt{div}\ \mathbf{h}_1 = 0, \tag{4.16}$$

where $\mathbf{S}_1$ and $\mathbf{h}_1$ represent the linearized Piola–Kirchhoff stress tensor and solvent flux, respectively. According to the neo-Hookean model, the non-vanishing components of the incremental stress tensor $\mathbf{S}_1 = -J_0 p_1 \mathbf{F}_0^{-T} - J_1 p_0 \mathbf{F}_0^{-T} + J_0 p_0 \mathbf{F}_0^{-T}\mathbf{F}_1^{T}\mathbf{F}_0^{-T} + G_d \mathbf{F}_1$ are

$$\mathbf{S}_{1_{RR}} = p_0 J_0^{-1} Q_0^{-4}(\partial_R u - Q^2 J_1) - p_1 Q_0^{-2} + G_d \partial_R u, \tag{4.17a}$$

$$\mathbf{S}_{1_{R\Theta}} = p_0 Q_0^{-1}\partial_R v + G_d R^{-1}(\partial_R u - v), \tag{4.17b}$$

$$\mathbf{S}_{1_{\Theta R}} = p_0 Q_0^{-1} R^{-1}(\partial_R u - v) + G_d \partial_R v, \tag{4.17c}$$

$$\mathbf{S}_{1_{\Theta\Theta}} = -Q_0(p_1 J_0 + p_0 J_1) + R^{-1}(G_d + J_0 p_0 Q_0^2)(u + \partial_\Theta v) \tag{4.17d}$$

and

$$\mathbf{S}_{1_{\Phi\Phi}} = -Q_0(p_1 J_0 + p_0 J_1) + R^{-1}(G_d + J_0 p_0 Q_0^2)(u + v\cot\Theta). \tag{4.17e}$$

Similarly, we consider the first-order perturbation $\mathbf{h}_1(R,\Theta)$ of the water flux, which, from equation (2.6), is $\mathbf{h}_1 = -\mathbf{M}_0\nabla\mu_1 - \mathbf{M}_1\nabla\mu_0$, where

$$\mathbf{M}_0 = \frac{D}{\mathcal{R}T}\frac{J_0-1}{\Omega}\mathbf{F}_0^{-2}, \tag{4.18}$$

$$\mathbf{M}_1 = \frac{D}{\mathcal{R}T\Omega}\mathbf{F}_0^{-1}[J_1\mathbf{I} - (J_0-1)(\mathbf{F}_1\mathbf{F}_0^{-1} + \mathbf{F}_0^{-1}\mathbf{F}_1^T)]\mathbf{F}_0^{-1} \tag{4.19}$$

and

$$\mu_1 = -\frac{\mathcal{R}T}{(J_0-1)J_0^3}[2\chi(J_0-1) - J_0]J_1 + \Omega p_1, \tag{4.20}$$

while $\mu_0(R)$ is given by equation (4.5). Consequently, the non-vanishing components of $\mathbf{h}_1$ are

$$h_{1_R} = -\frac{D}{\mathcal{R}T\Omega J_0^3 Q_0^6}[\mu_0' Q_0^2 J_0 J_1 + (J_0-1)(-2\mu_0'\partial_R u + J_0 Q_0^2 \partial_R \mu_1)] \tag{4.21a}$$

and

$$h_{1_\Theta} = \frac{D(J_0-1)}{\mathcal{R}T\Omega J_0^2 Q_0^3 R}[-J_0^2 Q_0^5 \partial_\Theta \mu_1 + \mu_0'(J_0 Q_0^3(\partial_\Theta u - v) + R\partial_R v)], \tag{4.21b}$$

and the incremental diffusion equation reduces to

$$\frac{1}{R^2}\partial_R(R^2 h_{1_R}) + \frac{1}{R\sin\Theta}\partial_\Theta(h_{1_\Theta}\sin\Theta) = 0. \tag{4.22}$$

The non-vanishing components of the incremental equilibrium equations (4.16) and the constraint equation (4.15) provide a system of four coupled partial differential equations for u, v, p_1 and J_1 as a function of R and Θ, where the coefficients depend on the finite-strain solution obtained at zeroth order.

To solve this problem, we expand the unknown fields in Legendre polynomials

$$u(R,\Theta) = \sum_{l=1}^{\infty}\mathcal{U}_l(R)\mathrm{P}_l(\cos\Theta),\ v(R,\Theta) = \sum_{l=1}^{\infty}\mathcal{V}_l(R)\partial_\Theta[\mathrm{P}_l(\cos\Theta)] \tag{4.23a}$$

and

$$p_1(R,\Theta) = \sum_{l=1}^{\infty}\mathcal{P}_l(R)\mathrm{P}_l(\cos\Theta),\ J_1(R,\Theta) = \sum_{l=1}^{\infty}\mathcal{J}_l(R)\mathrm{P}_l(\cos\Theta). \tag{4.23b}$$

We do not consider the mode $l=0$ in the expansions since it corresponds to a symmetric increase in shell radius and its existence does not correspond to a true axisymmetric bifurcation. By separation of variables, we obtain a system of ordinary differential equations for $\mathcal{U}_l$, $\mathcal{V}_l$, $\mathcal{P}_l$ and $\mathcal{J}_l$. This approach generalizes the classical ones for the stability of shells under pressure [20] and of growing shells [35].

We now use equation (4.15) to obtain

$$\mathcal{J}_l = R^{-1}J_0 Q_0[2\mathcal{U}_l - l(l+1)\mathcal{V}_l] + Q_0^{-2}\mathcal{U}_l', \tag{4.24}$$

and, therefore, eliminate $\mathcal{J}_l$ in the differential equations. Furthermore, to deal with (4.22) it is convenient, from a computational standpoint, to consider the following expansion for h_{1_R}

$$h_{1_R}(R,\Theta) = \sum_{l=1}^{\infty}\mathcal{H}_l(R)\mathrm{P}_l(\cos\Theta), \tag{4.25}$$

and solve the system of coupled equations in terms of $\{\mathcal{U}_l, \mathcal{U}_l', \mathcal{V}_l, \mathcal{V}_l', \mathcal{P}_l, \mathcal{H}_l\}$. More precisely, we introduce the vector $\mathbf{q}_l = \{\mathcal{U}_l, \mathcal{U}_l', \mathcal{V}_l, \mathcal{V}_l', \mathcal{P}_l, \mathcal{H}_l\}$ of the unknowns, so that our system of first-order linear differential equations is cast in the form

$$\mathbf{q}_l' = \mathbf{A}_l(R, Q_0(R), J_0(R), p_0(R))\mathbf{q}_l, \tag{4.26}$$

where $\mathbf{A}_l$ is the 6×6 coefficient matrix whose non-vanishing entries are reported in appendix B.

The linearized boundary conditions can be immediately derived by expanding (2.13), (2.14) to order $O(\epsilon)$ and by using (4.17), (4.20), (4.23), (4.24) and (4.25). By defining the functions

$$g(R) := \Omega \mathcal{P}_l - \frac{\mathcal{R}T(2\chi(J_0-1)-J_0)}{J_0^3(J_0-1)}[Q_0 J_0 R^{-1}(2\mathcal{U}_l - l(l+1)\mathcal{V}_l) + Q_0^{-2}\mathcal{U}_l'], \tag{4.27a}$$

$$f_R(R) := \mathcal{P}_l + G_d J_0 Q_0^5 R^{-1}[2\mathcal{U}_l - l(l+1)\mathcal{V}_l] - G_d Q_0^2 \mathcal{U}_l' \tag{4.27b}$$

and

$$f_\Theta(R) := -G_d(l+1)R^{-1}[J_0 Q_0^3(\mathcal{U}_l - \mathcal{V}_l) + R\mathcal{V}_l'], \tag{4.27c}$$

the boundary conditions can be written in the form

$$g(R_d) = 0, \quad f_R(R_d) = 0, \quad f_\Theta(R_d) = 0 \tag{4.28a}$$

and

$$g(R_c) - \Omega f_R(R_c) = 0, \quad f_\Theta(R_c) = 0. \tag{4.28b}$$

Equation (4.28*a*) represents the vanishing of the first-order chemical potential and first-order stress components at the external boundary. Similarly, $(4.28b)_2$ states the vanishing of the stress tangential component on the inner boundary. A more careful analysis is required for $(4.28b)_1$, which is derived from $(2.13)_2$. Actually, it comprises two separate boundary conditions, as we now discuss. Let us compute the cavity volume perturbation due to the displacement field (4.23). By using equation (2.17) to compute the cavity volume via Nanson's formula and using (4.13*a*), up to $O(\epsilon)$, we get

$$v_c = \frac{4}{3}\pi r_c^3 + \epsilon \frac{2}{3}\pi R_c^2 \int_0^\pi [(3u + \partial_\Theta v)\sin\Theta + v\cos\Theta]\, \mathrm{d}\Theta. \tag{4.29}$$

The substitution of (4.23) into (4.29) shows that to first order the perturbation of v_c vanishes, for any incremental displacement field. As a consequence, the inner pressure (the Lagrangian multiplier associated with the cavity volume constraint) also remains unchanged up to first order and implies $f_R(R_c) = 0$. Thus $(4.28b)_1$ can be replaced by the two conditions

$$g(R_c) = 0 \quad \text{and} \quad f_R(R_c) = 0. \tag{4.30}$$

In so doing, the system of six first-order linear equations (4.26) is complemented by the six boundary conditions (4.28*a*), $(4.28b)_2$ and (4.30).

(c) Critical volumes and bifurcation modes

We now consider the deformation of the spherical shell, when subject to the suction pressure due to the emptying of the inner cavity. When $\beta = v_c/v_{co}$ is larger than a critical value $\beta_c < 1$, the shell remains spherical; at β_c the shell buckles in a new state, and the spherical configuration becomes unstable. In mathematical terms, β_c is found by imposing that the equilibrium equations, linearized about the spherical configuration, show non-trivial solutions.

It is important to remark that, as already described in 4§b, the incremental equations are not easy to solve (despite being linear), because the coefficients are complicated functions of the zeroth-order solutions, which can only be found numerically. Furthermore, the critical parameter β appears explicitly only in the boundary conditions of the zeroth-order problem; see (4.10), (4.11) and (4.12). Therefore, the $O(1)$ and the $O(\epsilon)$ problems are coupled so that, in order to find the critical value β_c, we need to solve the zeroth-order equations (4.2), (4.6), (4.7) and (4.8) in the unknowns fields $(r(R), p_0(R), J_0(R))$ and the constant C_0 together with the first-order equations (4.26) in the unknowns $(\mathcal{U}_l, \mathcal{U}_l', \mathcal{V}_l, \mathcal{V}_l', \mathcal{P}_l, \mathcal{H}_l)$, simultaneously. To this end, let $\mathbf{y}_l = \{r, p_0, J_0, \mathcal{U}_l, \mathcal{U}_l', \mathcal{V}_l, \mathcal{V}_l', \mathcal{P}_l, \mathcal{H}_l\}$ be the vector of the unknowns, with l the order of the Legendre polynomials. The $O(1)$ and $O(\epsilon)$ system of ODEs can be written as a system of first-order equations of the form

$$\mathbf{y}_l' = \mathbf{f}(\mathbf{y}_l, R), \tag{4.31}$$

where R is the independent variable. The first three equations correspond to the spherical problem, they are nonlinear and affect the problem at order $O(\epsilon)$. By contrast, the remaining

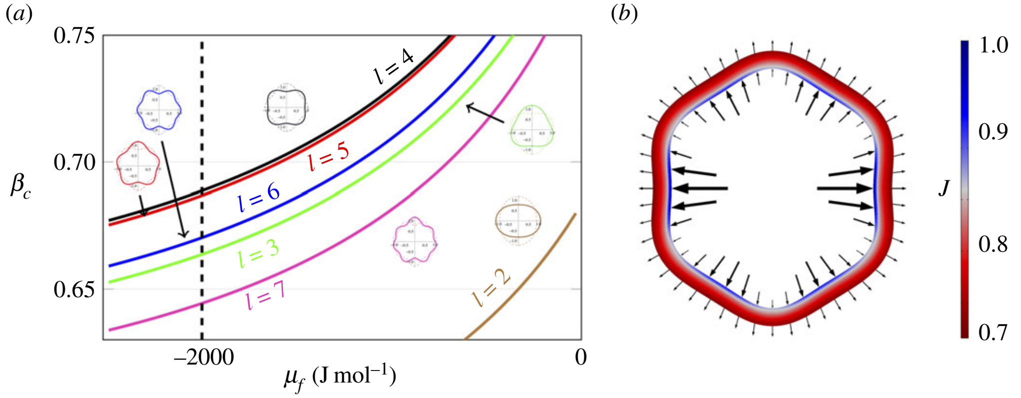

Figure 4. Critical ratio β_c versus μ_f. Each curve is associated with a bifurcation mode l: the order of the mode is written along the lines whereas the insets show the shapes corresponding to the modes. The vertical dashed line marks the value $\mu_f = -2000$ J/mol used in the numerical simulation (figure 2). The first bifurcation mode is given by the intersection of the vertical line at $\mu_f = -2000$ J mol^{-1} and the highest bifurcation curve corresponding to the highest critical threshold β_c, i.e. the critical value is the first met when emptying the cavity (*a*). Buckled shape evidenced in the numerical simulation corresponding to $\beta = 0.67$; the shape profile can be identified with the theoretical mode $l = 6$; the colour code refers to the ratio $J = J_d/J_o$ (*b*). (Online version in colour.)

six equations describe the linearized problem at order $O(\epsilon)$ and do not influence the zeroth-order problem. Furthermore, there are two additional unknown constants, namely the integration constant C_0 and the critical parameter β_c. Therefore, we need a total of 11 boundary conditions. Ten of these are given by equations (4.9), (4.11), (4.28*a*), (4.28*b*)$_2$ and (4.30). The eleventh boundary condition is $\mathcal{U}_l(R_c) = \bar{\mathcal{U}}$, with $\bar{\mathcal{U}} \neq 0$, and imposes a non-trivial solution on the problem. Since we deal with an eigenvalue problem, the particular choice of $\bar{\mathcal{U}}$ does not affect the result of the problem: the bifurcated solutions of the linearized problem are only known up to an arbitrary multiplicative factor [36].

Numerical integration is performed using the Matlab function `bvp4c`, which solves a boundary value problem by the collocation method. The critical thresholds β_c for various values of the final external chemical potential μ_f are computed by using the material parameter values from table 1 and the shell radius and thickness as in the numerical experiments presented in §3: $R_d = 10^{-2}$ m and $R_c/R_d = 0.875$.

Figure 4*a* shows the critical ratio β_c versus the external chemical potential μ_f. During the emptying process β decreases from the initial value $\beta = 1$ and, as already observed, the shell remains spherical until β reaches the critical value β_c, at which buckling occurs. Hence, during the emptying process, we expect to observe the bifurcation mode with the highest β_c, for the given external chemical potential μ_f. It is interesting to notice that, for fixed μ_f, the critical value β_c is not a strictly increasing function of the mode l but has a maximum for $l = 4$. By contrast, for a given mode l, β_c is an increasing function of μ_f. This means that, whereas instability occurs for values of μ_f closer to the initial value 0 J mol^{-1}, the cavity volume v_c will be closer to the initial value v_{co}.

It is worth noting that the linear analysis only qualitatively matches with the finite-element simulations. In fact, the predicted theoretical bifurcation mode ($l = 4$) at $\mu_f = -2000$ J mol^{-1} does not match with the numerical one ($l = 6$; see figure 4*b*). However, the theoretical $\beta_c = 0.67$ for $l = 6$ is in excellent agreement with the value $\beta_c = 0.68$ found in the numerical simulation (figure 2). The discrepancy between the predicted wavenumber might be due to the fact that the critical thresholds reported in figure 4 are very close to each other, and the system might be very sensitive to imperfections or initial conditions. Hence, stability and reliability of the numerical scheme are very difficult to achieve in this situation. In particular, *ad hoc* numerical schemes must be

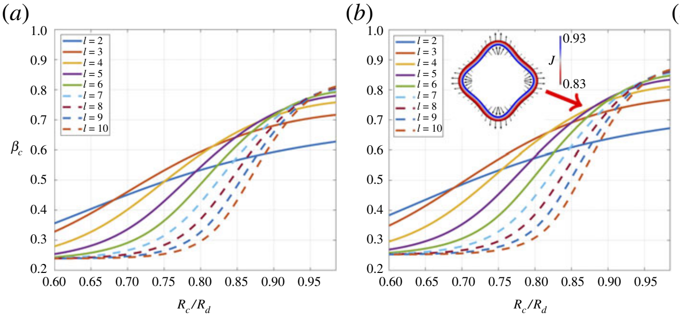

Figure 5. Critical ratio β_c versus R_c/R_d for the l-th buckling mode for $m \approx 0.37$ (*a*), $m \approx 0.55$ (*b*) and $m \approx 1.1$ (*c*). The inset in (*b*) shows the numerical buckled shape at $\beta = 0.74$; the colour code in the inset refers to the ratio $J = J_d/J_o$. (Online version in colour.)

implemented to prevent the numerical algorithm from trying to follow the spherical solution even when it is unstable, after the bifurcation has already taken place. Furthermore, it should be noted that we obtained the buckled shape corresponding to the mode $l = 4$ in a numerical simulation with $m = 0.55$ and $\beta \approx 0.74$, which agrees with the theoretical β_c, corresponding to $\mu_f = -2000\,\mathrm{J\ mol^{-1}}$, $m = 0.55$, by intersecting the vertical line at $R_c/R_d = 0.875$ with the curve $l = 4$. The numerical shape is shown as the inset in figure 5*b*.

Figure 5 shows the critical vale β_c versus the ratio R_c/R_d, for three values of m. It agrees with the classic results showing that thinner shells develop bifurcations at higher modes [26]. When m is sufficiently large, the capsules are relatively stiff and initially poorly swollen. In such a case, the bifurcation diagram agrees with fig. 9 in [26] (purely elastic case). By contrast, when m is smaller, the shell is softer and the bifurcation occurs at smaller cavity volume as all the curves shift downwards at $m = 0.37$ (figure 5*a*). The observed behaviour is in agreement with figure 3*d*, where it is shown that for increasing m the shell gets stiffer and volume changes are reduced (in the purely elastic case incompressibility requires $J = 1$).

5. Conclusion and future directions

We considered the instabilities of an elastic spherical shell that, starting from a fully hydrated state, shrinks during a dehydration process. A change in the external chemical potential triggers the process and induces the emptying of the spherical cavity confined by the shell, providing a negative pressure on the inner wall and, at the same time, the shrinking of the shell. When the cavity volume reaches a critical value, the shell buckles and loses its spherical shape. This phenomenon is captured by a finite-element simulation, which solves the coupled chemo-mechanical problem consisting in a stress-diffusion model based on the Flory–Rehner thermodynamics.

In order to understand how material and geometrical parameters affect the instability, we approximated the dynamical process as a sequence of equilibrium states over sufficiently small time intervals $\Delta t \ll \tau_d$, which holds in small diffusivity regimes. Over each interval, the volume cavity and the flux do not change with time and this allows us to solve the problem as a quasi-static problem where the cavity volume is prescribed.

Our analysis was inspired by other related works that dealt with the purely mechanical instability of elastic shells under pressure [20] or with the combined effect of pressure and differential growth [35]. However, a key and necessary ingredient of our analysis, which makes it different from previous studies, is the introduction of the diffusion equation. In fact, in our case, the mechanical and chemical problems are strongly coupled and the bifurcation occurs when the thermodynamical equilibrium has not been attained yet. Therefore, the chemo-mechanical problem is challenging for several reasons: (i) there is a larger number of state variables; (ii) the solution with spherical symmetry cannot be determined analytically; (iii) the local volumetric change in the spherical solution is not uniform in space and it is *a priori* unknown. We observe that a purely mechanical problem, with a neo-Hookean incompressible shell with fixed cavity volume, would lead to an overestimated critical value $\beta_c \approx 0.85$ as opposed to our $\beta_c \approx 0.67$ [26].

Despite the richness of the model, the perturbed solution still has a classical mathematical structure in that it can be decomposed into the product of radial functions and an angular function written in terms of Legendre polynomials. The thresholds obtained from the perturbative analysis successfully capture the instability observed in the finite-element model simulation. In particular, the critical threshold of mode $l = 6$, which corresponds to the simulated post-buckling shape, shows a good agreement between theoretical ($\beta_c \approx 0.67$) and numerical ($\beta_c \approx 0.68$) values.

We plan to perform a full exploration of the model parameters as a next step; in particular, the analysis of the instability under extreme environmental conditions such as in vacuum has also been planned. Finally, a simplified reduced model based on shell models with natural curvature, which would be related to the differential degree of hydration across the thickness of the shell, might be useful to advance the analytical treatment of the problem.

Data accessibility. This article has no additional data.

Authors' contributions. M.C.: conceptualization, formal analysis, investigation, methodology, project administration, visualization, writing–original draft, writing–review and editing. G.N.: conceptualization, formal analysis, investigation, methodology, project administration, visualization, writing–original draft, writing–review and editing. P.N.: conceptualization, formal analysis, investigation, methodology, project administration, visualization, writing–original draft, writing–review and editing. S.T.: conceptualization, formal analysis, investigation, methodology, project administration, visualization, writing–original draft, writing–review and editing.

Competing interests. We declare we have no competing interests.

Funding. The authors thank MIUR (Italian Minister for Education, Research and University) and *PRIN 2017, Mathematics of active materials: From mechanobiology to smart devices*, project no. 2017KL4EF3, for financial support and the National Group of Mathematical Physics (GNFM–INdAM) for support. M.C. acknowledges *PRIN 2017, Extra fast and accurate simulation of complex structural systems*, project no. 20173C478N and *PRIN 2017, Integrated mechanobiology approaches for a precise medicine in cancer treatment*, project no. 20177TTP3S for financial support. P.N. and M.C. thank MAECI (Italian Ministry for Foreign Affairs and International Cooperation) and the PAMM project for financial support.

Appendix A. Small and large diffusivity regimes

Given the system of equations (2.8)–(2.11), there are different characteristic times whose ratios affect the different solution regimes and are: the diffusion time $\tau_d = H_o^2/D$, the time τ_μ and the time τ_e needed to reach a thermodynamical equilibrium state. From the numerical solution of equations (2.8)–(2.11), we deduce that $\tau_d \dot{J}_d = \Omega \tau_d \dot{c}_d \simeq 0$; see figure 6*a*, where we represented the behaviour of $\tau_d ||\dot{J}_d||_\infty$ versus time. Hence, the concentration field c_d is nearly constant in time and it can be assumed that $\mathtt{div}\,\mathbf{h}_d = 0$. This allows us to approximate the dynamical process as a sequence of equilibrium problems which have different characteristics in the small and large diffusivity regimes, as we discuss below.

When we look at the solution for $t \simeq \tau_e \gg \tau_d$, that is, for large diffusivity D, all the fields have attained their thermodynamical equilibrium values. So, equation (2.19), under the spherical symmetry assumptions, delivers $h_{0_R}(R_c) = 0$ so that equation (4.7) yields $C_0 = 0$. Consequently, $h_{0_R}(R) = 0$ and $\mu(R) = \mu_e$. The other unknown fields $J_0(R)$, $p_0(R)$ and $r(R)$ can be determined by integrating equations (4.2), (4.6) and (4.7) with the boundary conditions (4.9*a*) at $R = R_d$ whereas at $R = R_c$ we have

$$\mu(R_c) = \mu_e \quad \text{and} \quad \frac{\mu_e}{\Omega} + Q_0^2(R_c) S_{0_{RR}}(R_c) = 0, \tag{A 1}$$

as $p_i = \mu_e/\Omega$. The sequence of equilibrium problems we solve is controlled by μ_e. If μ_e depends on time and its evolution is slow ($\tau_d/\tau_\mu \ll 1$), the approximation above holds and we get a *quasi-steady* solution of the problem; otherwise, if μ_e is constant, we get a *steady* solution.

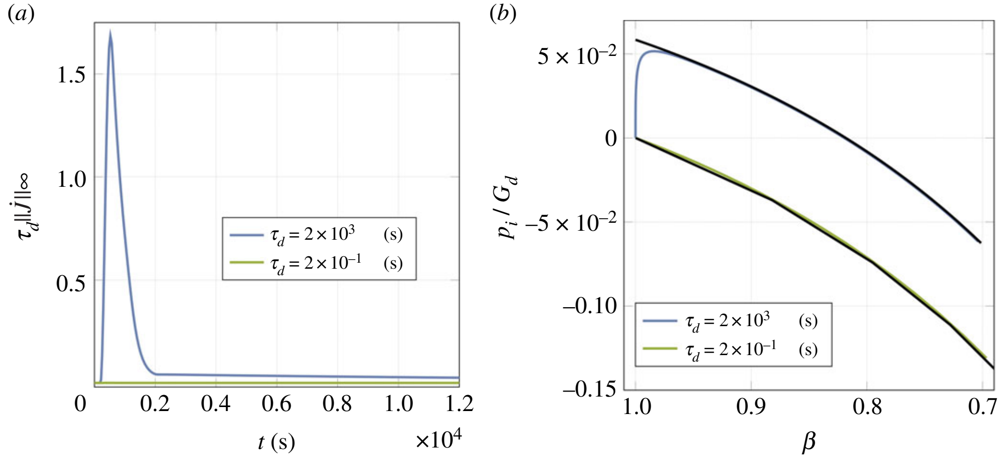

Figure 6. $\tau_d||\dot{J}||_\infty$ versus t lines for $\tau_d = 2 \times 10^3$ s (blue) and $\tau_d = 1.5 \times 10^{-1}$ s (green); the blue peak corresponds to the steep ramp of μ_e (*a*). Dimensionless pressure–volume curves p_i/G_d versus β from analytics (black) and numerics for $\tau_d = 2 \times 10^3$ s (blue) and $\tau_d = 1.5 \times 10^{-1}$ s (green) (*b*). (Online version in colour.)

The ratio β is determined as $r(R_c)^3/R_0^3$. The dimensionless pressure–volume curve p_i/G_d versus β in figure 6*b* (bottom black) shows the excellent agreement with the numerical curve (green).

By contrast, in the opposite regime, that is, when the diffusivity is small and we look at the solution for $t \ll \tau_e$ and $t > \tau_\mu$, which is the case we discussed in the paper, we approximate the dynamical process as a sequence of equilibrium states over sufficiently small time intervals $\Delta t \ll \tau_d$. Over each interval, the volume cavity and the flux do not change with time and this allows us to solve the problem by integrating equations (4.2), (4.6), (4.7) and (4.8) with the boundary conditions (4.9*a*), with $\mu_e = \mu_f$, and (4.9*b*). The sequence of equilibrium problems we solve is controlled by β and, at variance with the previous case, the cavity pressure p_i is an unknown of the problem. Figure 6 shows the dimensionless pressure–volume curve p_i/G_d versus β (top black) which, also in this case, is in excellent agreement with the numerical solution (blue).

Appendix B. Coefficients of the ODE system

We define

$$\mathcal{G}_0 := \frac{\mathrm{d}\mu_0}{\mathrm{d}J_0},$$

the non-vanishing coefficients of the linear system to solve are

$$A_{12} = 1,$$

$$A_{21} = \frac{G_d\,\Omega Q_0^3\{(J_0-1)[(2+l+l^2)Q_0 + 2\mathcal{R}\,T\,\mathcal{G}_0 J_0^2 Q_0^3] - 2R[(J_0-1)(\mathcal{R}T(J_0\mathcal{G}_0)' - \Omega p_0') + J_0\mu_0']\}}{(J_0-1)(\mathcal{R}\,T\,\mathcal{G}_0 + G_d\,\Omega Q_0^4)R^2},$$

$$A_{22} = \frac{-(J_0-1)[\mathcal{R}TJ_0(-2\mathcal{G}_0 + 4\mathcal{G}_0 Q_0^3 + \mathcal{G}_0' R) + 2\Omega\,G_d J_0 Q_0^4 - \mu_0' R] - \mu_0' R}{J_0(J_0-1)(\mathcal{R}T\mathcal{G}_0 + G_d\Omega Q_0^4)R},$$

$$A_{23} = \frac{-l(l+1)Q_0^3\{(J_0-1)[\mathcal{R}\,T(J_0^2 Q_0^3\mathcal{G}_0 - (J_0\mathcal{G}_0)'R) + 2\Omega(G_d Q_0 + p_0' R)] - J_0\mu_0' R\}}{(J_0-1)(\mathcal{R}\,T\,\mathcal{G}_0 + G_d\,\Omega Q_0^4)R^2},$$

$$A_{24} = \frac{l(l+1)\mathcal{R}\,T\,\mathcal{G}_0 J_0 Q_0^3}{R(\mathcal{R}\,T\,\mathcal{G}_0 + G_d \Omega Q_0^4)}, \qquad A_{26} = -\frac{\mathcal{R}\,T\,\Omega J_0^2 Q_0^6}{D(J_0-1)(\mathcal{R}\,T\,\mathcal{G}_0 + G_d \Omega Q_0^4)},$$

$$A_{34} = 1,$$

$$A_{41} = -\frac{2}{R^2} - \frac{p_0'}{G_d Q_0 R}, \qquad A_{43} = \frac{l(l+1)}{R^2} + \frac{p_0'}{G_d Q_0 R},$$

$$A_{44} = -\frac{2}{R}, \qquad A_{45} = \frac{Q_0 J_0}{G_d R},$$

$$\begin{aligned} A_{51} = {} & \big((J_0-1)(\mathcal{R}\,T\,\mathcal{G}_0 + G_d \Omega Q_0^4)R^2\big)^{-1}\{\mathcal{R}\,T\,\mathcal{G}_0 Q_0 (J_0-1) \\ & \times [-G_d Q_0(2 + l + l^2 - 2J_0^2 Q_0^6 + 2RQ_0^3 J_0') - 2p_0' R] - 2RG_d J_0 Q_0^5 [\mathcal{R}\,T\,(J_0-1)\mathcal{G}_0' + \mu_0']\}, \end{aligned}$$

$$A_{52} = \frac{G_d\, Q_0^2[-\mathcal{R}\,T\,J_0(J_0-1)(4\mathcal{G}_0(-1 + J_0 Q_0^3) + \mathcal{G}_0' R) + (-2+J_0)\mu_0' R]}{J_0(J_0-1)(\mathcal{R}\,T\,\mathcal{G}_0 + G_d\, \Omega Q_0^4)R},$$

$$\begin{aligned} A_{53} = {} & \big((J_0-1)(\mathcal{R}\,T\,\mathcal{G}_0 + G_d\, \Omega Q_0^4)R^2\big)^{-1}\{l(l+1)Q_0[\mathcal{R}\,T\,\mathcal{G}_0(J_0-1) \\ & \times (G_d\, Q_0(2 - J_0^2 Q_0^6 + Q_0^3 J_0' R) + p_0' R) + RG_d\, J_0 Q_0^4(\mathcal{R}\,T\,(J_0-1)\mathcal{G}_0' + \mu_0')]\}, \end{aligned}$$

$$A_{54} = \frac{l(l+1)\mathcal{R}\,T\,G_d\,\mathcal{G}_0 J_0 Q_0^5}{(\mathcal{R}\,T\,\mathcal{G}_0 + G_d\, \Omega Q_0^4)R}, \quad A_{56} = -\frac{\mathcal{R}\,T\,G_d\, \Omega J_0^2 Q_0^8}{D(J_0-1)(\mathcal{R}\,T\,\mathcal{G}_0 + G_d\, \Omega Q_0^4)},$$

$$A_{61} = \frac{D\, l(l+1)(J_0-1)(-2\mathcal{R}\,T\mathcal{G}_0 J_0^2 Q_0^3 + \mu_0' R)}{\Omega J_0 \mathcal{R}\,TR^3}, \quad A_{62} = -\frac{D\,\mathcal{G}_0\, l(l+1)(J_0-1)}{\Omega\, R^2},$$

$$A_{63} = \frac{D\, l(l+1)(J0-1)[l(l+1)\mathcal{R}\,T\,\mathcal{G}_0 J_0^2 Q_0^3 - \mu_0' R]}{\Omega \mathcal{R}\,T J_0 R^3},$$

$$A_{64} = \frac{D\, l(l+1)(J_0-1)\mu_0'}{\Omega \mathcal{R}\,T J_0^2 Q_0^3 R}, \quad A_{65} = -\frac{D\, l(l+1)(J_0-1)Q_0^2}{\mathcal{R}\,TR^2}.$$

References

1. Noblin X, Rojas NO, Westbrook J, Llorens C, Argentina M, Dumais J. 2012 The fern sporangium: a unique catapult. *Science* **335**, 1322–1322. (doi:10.1126/science.1215985)
2. Llorens C, Argentina M, Rojas N, Westbrook J, Dumais J, Noblin X. 2016 The fern cavitation catapult: mechanism and design principles. *J. R. Soc. Interface* **13**, 20150930. (doi:10.1098/rsif.2015.0930)
3. Whitaker DL, Edwards J. 2010 Sphagnum moss disperses spores with vortex rings. *Science* **329**, 406–406. (doi:10.1126/science.1190179)
4. Sakes A, van der Wiel M, Henselmans PWJ, van Leeuwen JL, Dodou D, Breedveld P. 2016 Shooting mechanisms in nature: a systematic review. *PLoS ONE* **11**, e0158277. (doi:10.1371/journal.pone.0158277)
5. Lucantonio A, Nardinocchi P, Teresi L. 2013 Transient analysis of swelling-induced large deformations in polymer gels. *J. Mech. Phys. Solids* **61**, 205–218. (doi:10.1016/j.jmps.2012.07.010)
6. Lucantonio A, Roche M, Nardinocchi P, Stone HA. 2014 Buckling dynamics of a solvent-stimulated stretched elastomeric sheet. *Soft Matter* **10**, 2800–2804. (doi:10.1039/c3sm52941j)
7. Lucantonio A, Nardinocchi P, Stone HA. 2014 Swelling dynamics of a thin elastomeric sheet under uniaxial pre-stretch. *J. Appl. Phys.* **115**, 083505. (doi:10.1063/1.4866576)
8. Curatolo M, Nardinocchi P, Teresi L. 2018 Driving water cavitation in a hydrogel cavity. *Soft Matter* **14**, 2310–2321. (doi:10.1039/C8SM00100F)
9. Curatolo M, Nardinocchi P. 2018 Swelling-induced bending and pumping in homogeneous thin sheets. *J. Appl. Phys.* **124**, 085108. (doi:10.1063/1.5043580)
10. Mora T, Boudaoud A. 2006 Buckling of swelling gels. *Eur. Phys. J. E* **20**, 119–124. (doi:10.1140/epje/i2005-10124-5)
11. Kang MK, Huang R. 2010 Swell-induced surface instability of confined hydrogel layers on substrates. *J. Mech. Phys. Solids* **58**, 1582–1598. (doi:10.1016/j.jmps.2010.07.008)

12. Li K, Ding K, Cai S. 2013 Diffusion-induced wrinkling instability in a circular poroelastic plate. *Appl. Phys. Lett.* **102**, 241908. (doi:10.1063/1.4811753)
13. Weiss F, Cai S, Hu Y, Kang MK, Huang R, Suo Z. 2013 Creases and wrinkles on the surface of a swollen gel. *J. Appl. Phys.* **114**, 073507. (doi:10.1063/1.4818943)
14. Pandey A, Holmes DP. 2013 Swelling-induced deformations: a materials-defined transition from macroscale to microscale deformations. *Soft Matter* **9**, 5524–5528. (doi:10.1039/C3SM00135K)
15. Toh W, Ding Z, Yong Ng T, Liu Z. 2015 Wrinkling of a polymeric gel during transient swelling. *J. Appl. Mech.* **82**, 0 61 004–0 61 012. (doi:10.1115/1.4030327)
16. Takahashi R, Ikura Y, King DR, Nonoyama T, Nakajima T, Kurokawa T, Kuroda H, Tonegawa Y, Gong JP. 2016 Coupled instabilities of surface crease and bulk bending during fast free swelling of hydrogels. *Soft Matter* **12**, 5081–5088. (doi:10.1039/C6SM00578K)
17. Bertrand T, Peixinho J, Mukhopadhyay S, MacMinn CW. 2016 Dynamics of swelling and drying in a spherical gel. *Phys. Rev. Appl.* **6**, 064010. (doi:10.1103/PhysRevApplied.6.064010)
18. Curatolo M, Nardinocchi P, Puntel E, Teresi L. 2017 Transient instabilities in swelling dynamics. (http://arxiv.org/abs/1704.08201)
19. Green AE, Rivlin RS, Shield RT, Goldsbrough GR. 1952 General theory of small elastic deformations superposed on finite elastic deformations. *Proc. R. Soc. Lond. A* **211**, 128–154. (doi:10.1098/rspa.1952.0030)
20. Wesolows Z. 1967 Stability of an elastic, thick-walled spherical shell loaded by an external pressure. *Archiwum Mechaniki Stosowanej* **1**, 3–22.
21. Haughton D, Ogden R. 1978 On the incremental equations in non-linear elasticity—II. Bifurcation of pressurized spherical shells. *J. Mech. Phys. Solids* **26**, 111–138. (doi:10.1016/0022-5096(78)90017-0)
22. Hutchinson JW. 2016 Buckling of spherical shells revisited. *Proc. R. Soc. A* **472**, 20160577. (doi:10.1098/rspa.2016.0577)
23. Pezzulla M, Stoop N, Steranka MP, Bade AJ, Holmes DP. 2018 Curvature-induced instabilities of shells. *Phys. Rev. Lett.* **120**, 048002. (doi:10.1103/PhysRevLett.120.048002)
24. Holmes DP, Lee JH, Park HS, Pezzulla M. 2020 Nonlinear buckling behavior of a complete spherical shell under uniform external pressure and homogenous natural curvature. *Phys. Rev. E* **102**, 023003. (doi:10.1103/PhysRevE.102.023003)
25. Knoche S, Kierfeld J. 2014 Osmotic buckling of spherical capsules. *Soft Matter* **10**, 8358–8369. (doi:10.1039/C4SM01205D)
26. Ben Amar M, Goriely A. 2005 Growth and instability in elastic tissues. *J. Mech. Phys. Solids* **53**, 2284–2319. (doi:10.1016/j.jmps.2005.04.008)
27. Goriely A, Ben Amar M. 2005 Differential growth and instability in elastic shells. *Phys. Rev. Lett.* **94**, 198103. (doi:10.1103/PhysRevLett.94.198103)
28. Flory PJ, Rehner J. 1943 Statistical mechanics of cross-linked polymer networks I. Rubberlike elasticity. *J. Chem. Phys.* **11**, 512–520. (doi:10.1063/1.1723791)
29. Flory PJ, Rehner J. 1943 Statistical mechanics of cross-linked polymer networks II. Swelling. *J. Chem. Phys.* **11**, 521–526. (doi:10.1063/1.1723792)
30. Hong W, Zhao X, Zhou J, Suo Z. 2008 A theory of coupled diffusion and large deformation in polymeric gels. *J. Mech. Phys. Solids* **56**, 1779–1793. (doi:10.1016/j.jmps.2007.11.010)
31. Zhang J, Zhao X, Suo Z, Jiang H. 2009 A finite element method for transient analysis of concurrent large deformation and mass transport in gels. *J. Appl. Phys.* **105**, 093522. (doi:10.1063/1.3106628)
32. Chester SA, Anand L. 2010 A coupled theory of fluid permeation and large deformations for elastomeric materials. *J. Mech. Phys. Solids* **58**, 1879–1906. (doi:10.1016/j.jmps.2010.07.020)
33. Curatolo M, Nardinocchi P, Teresi L. 2020 Modeling solvent dynamics in polymers with solvent-filled cavities. *Mech. Soft Mater.* **2**, 1–16. (doi:10.1007/s42558-020-00029-0)
34. Li J, Suo Z, Vlassak JJ. 2014 Stiff, strong, and tough hydrogels with good chemical stability. *J. Mater. Chem. B* **2**, 6708–6713.
35. Goriely A. 2017 *The mathematics and mechanics of biological growth*. New York, NY: Springer.
36. Ambrosetti A, Prodi G. 1995 *A primer of nonlinear analysis*. Cambridge, UK: Cambridge University Press.